Naval Research Laboratory

Washington, DC 20375-5000

NRL Memorandum Report 6390

Radio Frequency Linac Driven Free-Electron Laser Configurations

C.M. TANG, P. SPRANGLE, A. TING AND B. HAFIZI*

Beam Physics Branch
Plasma Physics Division

**Science Applications Intl. Corp.*
McLean, VA

September 7, 1989

Approved for public release; distribution unlimited.

SECURITY CLASSIFICATION OF THIS PAGE

REPORT DOCUMENTATION PAGE

Form Approved
OMB No. 0704-0188

1a. REPORT SECURITY CLASSIFICATION UNCLASSIFIED	1b. RESTRICTIVE MARKINGS
2a. SECURITY CLASSIFICATION AUTHORITY	3. DISTRIBUTION/AVAILABILITY OF REPORT Approved for public release; distribution unlimited.
2b. DECLASSIFICATION/DOWNGRADING SCHEDULE	
4. PERFORMING ORGANIZATION REPORT NUMBER(S) NRL Memorandum Report 6390	5. MONITORING ORGANIZATION REPORT NUMBER(S)
6a. NAME OF PERFORMING ORGANIZATION Naval Research Laboratory 6b. OFFICE SYMBOL (If applicable) Code 4790	7a. NAME OF MONITORING ORGANIZATION
6c. ADDRESS (City, State, and ZIP Code) Washington, DC 20375-5000	7b. ADDRESS (City, State, and ZIP Code)
8a. NAME OF FUNDING/SPONSORING ORGANIZATION Office of Naval Research 8b. OFFICE SYMBOL (If applicable)	9. PROCUREMENT INSTRUMENT IDENTIFICATION NUMBER
8c. ADDRESS (City, State, and ZIP Code) Arlington, VA 22217	10. SOURCE OF FUNDING NUMBERS PROGRAM ELEMENT NO. / PROJECT NO. / TASK NO / WORK UNIT ACCESSION NO.

11. TITLE (Include Security Classification)
Radio Frequency Linac Driven Free-Electron Laser Configurations

12. PERSONAL AUTHOR(S)
Tang, C.M., Sprangle, P., Ting, A. and Hafizi,* B.

13a. TYPE OF REPORT	13b. TIME COVERED	14. DATE OF REPORT (Year, Month, Day)	15. PAGE COUNT
Interim	FROM _____ TO _____	1989 September 7	34

16. SUPPLEMENTARY NOTATION
*Science Application Intl. Corp., McLean, VA

17. COSATI CODES			18. SUBJECT TERMS (Continue on reverse if necessary and identify by block number)
FIELD	GROUP	SUB-GROUP	FEL SSPA MOPA

19. ABSTRACT (Continue on reverse if necessary and identify by block number)

Recent developments in accelerator technology and the optical guiding property of the free electron laser (FEL) radiation indicate that the RF linacs may be a strong contender for driving high average power FEL amplifiers. We discuss two RF linac driven FEL configurations: the master oscillator power amplifier (MOPA) and the single stage power amplifier (SSPA). Our numerical results are obtained using the source dependent expansion (SDE) method in the computer code SHERA. The SDE method and the code SHERA are discussed and illustrations of the MOPA and SSPA configurations presented.

20. DISTRIBUTION/AVAILABILITY OF ABSTRACT	21. ABSTRACT SECURITY CLASSIFICATION
☒ UNCLASSIFIED/UNLIMITED ☐ SAME AS RPT ☐ DTIC USERS	UNCLASSIFIED
22a. NAME OF RESPONSIBLE INDIVIDUAL C.M. Tang	22b. TELEPHONE (Include Area Code) (202) 7674148 22c. OFFICE SYMBOL Code 4790

DD Form 1473, JUN 86 *Previous editions are obsolete.* SECURITY CLASSIFICATION OF THIS PAGE

S/N 0102-LF-014-6603

CONTENTS

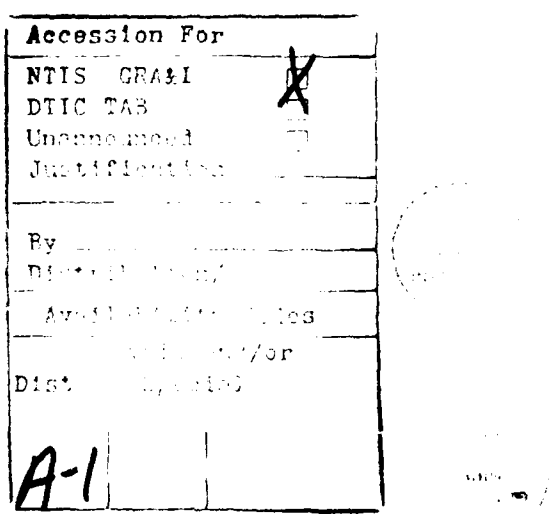

RADIO FREQUENCY LINAC DRIVEN FREE-ELECTRON LASER CONFIGURATIONS

Introduction

Significant advances in radio frequency (RF) linac technology concerning the reduction of emittance and increase in beam current have been taking place. Lower emittance allows for a smaller electron beam radius and thus higher current densities and laser gain. Under appropriate conditions, the radiation generated in a free electron laser (FEL) can be focused and overcome the natural tendency to diffract (spread transversely). This optical guiding phenomenon was first analyzed in the low gain regime[1], and later in the exponential gain regime[2-7]. Optical guiding in the FEL can enhance the gain and efficiency and is an integral part of the configurations illustrated in this paper.

We have presented a formalism for describing the three-dimensional radiation field in FELs called the source dependent expansion (SDE) method[6-7]. In this approach, the radiation field is decomposed into a sum of complete normal modes. Instead of using the usual modal expansion consisting of vacuum Gaussian Laguerre functions, the SDE method incorporates the source function (driving current) self-consistently into the functional dependence of, i) the radiation waist, ii) the radiation wavefront curvature and iii) the complex radiation amplitude. The SDE method significantly reduces the number of modes that are required to model the radiation field and reduces the computational time and cost of the simulations.

In our numerical examples the electron dynamics include: i) betatron oscillations, ii) finite emittance and iii) energy spread. The FEL equations together with the SDE method

Manuscript approved July 24, 1989.

are implemented in the computer code SHERA. The code is applied to the analysis of high extraction FELs driven by RF linacs. Two FEL configurations, which we considered, are the i) master oscillator power amplifier (MOPA) and ii) single stage power amplifier (SSPA). The schematic configurations are shown in Fig. 1. In both of those configurations, optical guiding plays a central role.

The Formulation of 3-D FEL Equations

We will consider a realistic, linearly polarized wiggler expressed in terms of the vector potential,

$$\mathbf{A}_w(x,y,z) = A_x(x,y,z)\cos(\int_0^z k_w(z')dz')\hat{e}_x, \tag{1}$$

where $A_x(x,y,z)$ and $k_w(z)$ are slowly varying functions of z. The expressions for $A_x(x,y,z)$ takes on different forms depending on the shape of the magnetic pole face.

The linearly polarized radiation field is

$$\mathbf{A}_R(r,\theta,z,t) = -A(r,\theta,z)\exp[i\omega(z/c-t)]\hat{e}_x/2 + c.c., \tag{2}$$

where $A(r,\theta,z) = |A(r,\theta,z)|e^{i\phi(r,\theta,z)}$ is the complex amplitude of the radiation field expressed in polar variables, ω is the frequency, and c.c. denotes the complex conjugate.

The wave equation governing $\mathbf{A}_R$ is

$$\left(\frac{1}{r}\frac{\partial}{\partial r}r\frac{\partial}{\partial r} + \frac{1}{r^2}\frac{\partial^2}{\partial\theta^2} + \frac{\partial^2}{\partial z^2} - \frac{1}{c^2}\frac{\partial^2}{\partial z^2}\right)\mathbf{A}_R = -\frac{4\pi}{c}J_x\hat{\mathbf{e}}_x, \tag{3}$$

where J_x is the driving current density. The detailed representaion for the current is given in Ref. 8. Using the SDE method[6-7], the radiation field is represented in the form,

$$A(r,\theta,z) = \sum_{m,p} C_{m,p}(\theta,z)D_m^p(r,z). \tag{4a}$$

where

$$\frac{|e|}{\sqrt{2}m_0c^2}C_m^p(\theta,z) = a_{m,p}(z)\cos(p\theta) + b_{m,p}(z)\sin(p\theta), \tag{4b}$$

$$D_m^p(\xi) = \frac{2}{r_s(z)}\left(\frac{m!}{(m+p)!}\right)^{1/2}\xi^{p/2}L_m^p(\xi)\exp[-(1-i\alpha(z))\xi/2], \tag{4c}$$

$$\xi = \frac{2r^2}{r_s^2(z)}, \tag{4d}$$

and

$$\int_0^\infty D_m^p(\xi)\,[D_n^p(\xi)]^*\,r dr = \delta_{m,p}. \tag{4e}$$

The functional dependence of the spot size r_s and curvature α are governed by the driving current.

Multiplying both sides of Eq. (3) by $\exp[i(\omega(z/c - t)]$ and integrating over t, from 0 to $2\pi/\omega$, then multiplying both sides by $D_m^p \cos(p\theta)$ or $D_m^p \sin(p\theta)$ and integrating over r, from 0 to ∞, yields the following SDE equations governing the radiation field,

$$\left[\frac{\partial}{\partial z} + Q_{m,p}(z)\right]\begin{bmatrix} a_{m,p}(z) \\ b_{m,p}(z)\end{bmatrix} - i\sqrt{m(m+p)}B(z)\begin{bmatrix} a_{m-1,p}(z) \\ b_{m-1,p}(z)\end{bmatrix}$$

$$-i\sqrt{(m+1)(m+p+1)}B^*(z)\begin{bmatrix} a_{m+1,p}(z) \\ b_{m+1,p}(z)\end{bmatrix} = -i\begin{bmatrix} F_{m,p}(z) \\ G_{m,p}(z)\end{bmatrix}, \tag{5}$$

where

$$Q_{m,p}(z) = \frac{r_s'}{r_s} + i(2m+p+1)\left[\frac{c}{\omega}\frac{(1+\alpha^2)}{r_s^2} - \alpha\frac{r_s'}{r_s} + \frac{\alpha'}{2}\right], \tag{6}$$

$$B(z) = -\left[\alpha\frac{r_s'}{r_s} + \frac{c}{\omega}\frac{(1-\alpha^2)}{r_s^2} - \frac{\alpha'}{2}\right] - i\left[\frac{r_s'}{r_s} - 2\frac{c}{\omega}\frac{\alpha}{r_s^2}\right], \tag{7}$$

$$\begin{bmatrix} F_{m,p} \\ G_{m,p}\end{bmatrix} = \kappa\left(\frac{1}{1+\delta_{p,0}}\right)\left\langle \frac{a_w(\tilde{x},\tilde{y},z)[\tilde{D}_m^p]^* e^{-i(\psi-\tilde{\phi})}}{\tilde{\gamma}\tilde{\beta}_z}\begin{bmatrix}\cos p\tilde{\theta} \\ \sin p\tilde{\theta}\end{bmatrix}\right\rangle, \tag{8}$$

where $\kappa = (1/2)(\omega_b^2/c^2)(c/\omega)F_B\sigma_b$, "$\sim$" on top of a quantity denotes the instantaneous values of the variable of a given particle at the axial position z, * denotes the complex conjugate and the prime denotes a derivative with respect to z, i.e., $' = \partial/\partial z$. In addition, $a_w = (|e|/\sqrt{2}m_0c^2)A_x$ is the normalized wiggler amplitude, $F_B = J_0(b) - J_1(b)$ for a linearly polarized wiggler, $b = a_w(0,0,z)^2/2(1+a_w(0,0,z)^2)$, σ_b is the effective area associated with the transverse electron beam profile, $\omega_b = (4\pi|e|^2 n_0/m_0c^2)^{1/2}$ is the plasma frequency of

the electron beam on axis, $\delta_{p,0} = 1$ for $p = 0$, and $\delta_{p,0} = 0$, otherwise. The symbol $\langle\rangle$ denotes the average

$$\langle(...)\rangle = \int_0^{2\pi} \frac{d\psi_0}{2\pi} \int dx_0 \int dy_0 \int dp_{x0} \int dp_{y0} \int dp_{z0} f_o(\psi_0, x_0, y_0, p_{x0}, p_{y0}, p_{z0})(...), \quad (9)$$

and is the integral over all the various initial conditions at $z = 0$, where f_o is the initial electron beam distribution function and f_o is normalized such that $< (1) >= 1$. For a parabolic transverse electron beam profile, $\sigma_b = \pi(r_b^2/2)$, and $\kappa = \nu(c/\omega)F_B$, where $\nu = \omega_b^2\sigma_b/4\pi c^2 \simeq I(A)/17 \times 10^3$ is Budker's constant and r_b is the edge radius of the electron beam.

The radiation amplitude evolves as electrons move in the longitudinal ponderomotive potential field formed by the beating of the wiggler field and the radiation field. The electron's phase in the ponderomotive potential field is defined as ψ, where

$$\psi(z; \psi_0, x_0, y_0, p_{x0}, p_{y0}, p_{z0}) = \int_0^z \left(\frac{\omega}{c} + k_w(z') - \frac{\omega}{\bar{v}_z(z')}\right) dz' + \bar{\phi} + \psi_0, \quad (10)$$

ψ_0 is the initial phase in the ponderomotive potential well, (x_0, y_0) are the initial transverse positions, (p_{x0}, p_{y0}) are the initial transverse momentum and p_{z0} is the initial axial momentum.

At this point in the SDE analysis, the function $H(z)$ is arbitrary. If $H(z)$ is not specified, the equations for $a_{m,p}$ and $b_{m,p}$ in (5) are underdetermined, i.e., there are more equations than unknowns. The SDE method provides a representation for r_s and α that yields analytical results and minimizes the numerical computation in a fully self-consistent simulation. It is assumed that the radiation beam profile remains approximately Gaussian with a nearly circular cross section. In this case we expect the magnitude of the coefficients, $a_{m,p}(z)$ and $b_{m,p}(z)$ to become progressively smaller as m and p take on larger values. Hence, if the lowest order mode $a_{0,0}$ gives a rough approximation to the radiation field, we may solve for $a_{0,0}(z)$, $r_s(z)$ and $\alpha(z)$. We find

$$(\partial/\partial z + Q_{0,0})a_{0,0} \simeq -iF_{0,0}, \quad (11)$$

and

$$B \simeq F_{1,0}/a_{0,0}. \quad (12)$$

Equation (12) above yields the following first order coupled differential equation for $r_s(z)$ and $\alpha(z)$,

$$r_s' - 2\frac{c}{\omega}\frac{\alpha}{r_s} = -\frac{r_s}{a_{0,0}}\left(F_{1,0}\right)_I, \tag{13a}$$

$$\alpha' - 2\frac{c}{\omega}\frac{(1+\alpha^2)}{r_s^2} = \frac{2}{a_{0,0}}\left[\left(F_{1,0}\right)_R - \alpha\left(F_{1,0}\right)_I\right], \tag{13b}$$

where $()_{R,I}$ denotes the real and imaginary parts of the enclosed function. In the SDE method, the function $H(z)$ is specified by (13).

The particle motion in the z-direction is best written in terms of the equation for the phase ψ and the total relativistic gamma,

$$\frac{d\gamma}{dz} = -\frac{\omega/c}{\tilde{\gamma}} F_B \tilde{a}_w(\tilde{x},\tilde{y},z)|a(\tilde{x},\tilde{y},z)|\sin\psi, \tag{14}$$

and

$$\frac{d(\psi-\tilde{\phi})}{dz} = -k_w(0)\frac{\omega/c(1+\tilde{a}_w(\tilde{x},\tilde{y},z)^2)}{\tilde{\beta}_z(1+\tilde{\beta}_z)\tilde{\gamma}^2} + k_w(z), \tag{15}$$

where $\beta_z = v_z/c$.

Description of the 3-D FEL Code SHERA

SHERA is a steady-state, single frequency code, which uses the SDE method to evaluate the radiation beam in the FEL. It incorporates realistic wiggler effects, such as transverse gradient and wiggler noise. In the results presented here, the wiggler is assumed to be free of field errors and it has weak focusing in both the x and y planes via parabolic pole peices[9], i.e.,

$$A_x(x,y,z) = A_w(z)\cosh(k_{w,x}x)\cosh(k_{w,y}y), \tag{16}$$

where $k_{w,x}^2 + k_{w,y}^2 = k_w^2$. For equal focusing in the x and y plane implies, $k_{w,x} = k_{w,y}$.

The wiggler field can be tapered by assigning a functional form for $k_w(z)$, $a_w(z)$ or resonant phase associated with a test particle. The resonant phase is defined as the phase associated with the bottom of the ponderomotive potential well, $\psi_R = constant$. A test particle trapped at the resonant phase satisfies the following equation

$$\frac{d^2\psi_R}{dz^2} = 0 = T(z) - \tilde{K}_s^2\sin\psi_R, \tag{17}$$

where

$$T(z) = \frac{dk_w}{dz} - \frac{\omega/c}{2\bar{\gamma}^2}\frac{d\bar{a}_w^2}{dz},$$

and $\bar{K}_s^2 = \left((1+\bar{a}_w^2)/\bar{\gamma}^4\right)(\omega/c)^2 F_B \bar{a}_w|\bar{a}|$ is the synchrotron wave number, where "–" denotes the value associated with the test particle.

For simplicity, the electron distribution function is assumed to be separable in this paper, i.e., $f_o = f_p(\psi_0) f_\epsilon(x_0, y_0, p_{x0}, p_{y0}) f_z(p_{z0})$. The initial transverse electron beam distribution is assumed to have a water bag distribution, i.e., the electron density is

$$f_\epsilon = \begin{cases} 1/V & R_b < r_b, \\ 0 & R_b > r_b, \end{cases} \tag{18}$$

where $R_b^2 = x_0^2 + y_0^2 + (v_{x0}^2 + v_{y0}^2)/(k_\beta(0)c)^2$ is the radius in the emittance space, V is the 4-dimensional phase space volume and $\tilde{k}_\beta = a_w(\bar{x}, \bar{y}, z)k_w/\tilde{\gamma}$ is the betatron wave number for a parabolic pole face with equal focusing in both the x and y planes. Integrated over the transverse velocity, the electron beam has a parabolic density profile with the beam density n_0 on axis where r_b is the beam edge radius.

The transverse motion of the electrons due to finite emittance in the realistic wiggler can be expressed accurately by an analytical expression for $yk_w << 1$. The particle motion is approximately,

$$\begin{bmatrix} \tilde{x} \\ \tilde{y} \end{bmatrix} = \left(\frac{\tilde{k}_\beta(0)}{\tilde{k}_\beta(z)}\right)^{1/2} \begin{bmatrix} x_0 \cos\tilde{\Phi} + v_{x0}\sin\tilde{\Phi} \\ y_0 \cos\tilde{\Phi} + v_{y0}\sin\tilde{\Phi} \end{bmatrix}, \tag{19}$$

where $\tilde{\Phi} = \int_0^z k_\beta(z')dz'$.

In the following simulations, the electron beam is matched at the entrance of the wiggler, i.e., the electron beam radius inside the wiggler is uniform if the wiggler parameters are constant. The matching condition becomes

$$r_b = \left(\frac{\lambda_w(0)\epsilon_n}{\pi a_w}\right)^{1/2}, \tag{20}$$

where λ_w is the wavelength of the wiggler, ϵ_n is the normalized beam edge emittance, $\pi\epsilon_n/\beta\gamma$ is the electron beam area in transverse phase space.

The beam current is modeled by discrete macro particles. To minimize the number of electrons in the simulation, the integrals over the initial conditions are performed

by quadratures. Gaussian quadrature is used for the initial phase ψ_0 and a 72 point quadrature[10] is used for the 4-dimensional transverse emittance. The energy spread is modeled by Gaussian, top-hat or any prescribed distribution functions, and implemented by either evenly spaced grids, or Gaussian quadrature. For simulations in this paper, the full interval of the Gaussian quadrature for the energy spread is 1.25 times the Gaussian width.

RF Linac Driven Power Amplifiers

RF linacs have only been used as drivers for FEL oscillators due to low gain. Because of significant continuous advances in reducing beam emittance and increasing beam current, i.e., high beam brightness, RF linacs appear to be suitable to drive FEL amplifiers. With the improvement in electron beam brightness, the high power FEL oscillator configuration becomes less attractive, mainly because of the problem of mirror damage. In this paper we present two configurations which can achieve high gain and high efficiency. These are the master oscillator power amplifier (MOPA) and the single stage power amplifier (SSPA) configurations.

I. Master Oscillator Power Amplifier (MOPA)

The MOPA concept, Fig. 1a, consists of trapping the electrons in the ponderomotive potential well and tapering the wiggler from the entrance to the exit of the wiggler for efficiency enhancement. To create a large ponderomotive potential well requires high power input radiation from a master oscillator. The large input laser can be an FEL oscillator. We will give an example of an RF linac that will produce 1 μm radiation in the MOPA configuration with high efficiency and high power. The parameters of the wiggler, the input radiation and the electron beam are given in Table I.

The electron beam has an energy of 140 MeV, a peak current of 500 A, an intrinsic energy spread of 1.0% FWHM, a normalized edge emittance of $\epsilon_n = 0.008\ cm - rad$ and a beam brightness of $B = 1.3 \times 10^{10}\ A/(m - rad)^2$. These parameters are not too different from the existing RF linac beam at Boeing Aerospace Company.

The amplitude of the vector potential of the wiggler is tapered for efficiency enhancement, see Fig. 2. The taper is slow initially and becomes faster at the end of the wiggler. If all the electrons are trapped, the maximum efficiency would be 15.8%.

The following simulation results are obtained with an injected radiation that is focused at the entrance of the wiggler with a flat wavefront. The efficiency and radiation guiding can be further improved by moving the focal point, but will not be presented here.

For an input radiation power of 50 MW, focused to a spot size of 0.1 cm, the fractional trapping potential is

$$\frac{|e|\phi_{trap}}{\gamma m_0 c^2} = 4\left(\frac{a_w a_{00}}{1+a_w^2}\right)^{1/2} = 1.6\%. \tag{21}$$

The estimate of the trapping protential has to be adjusted by the initial resonant phase, which is $\sin\psi_R = 0.25$. The actual trapping potential is sufficient for trapping an electron beam with a 1.0% energy spread. Since the radiation grows rapidly, some of the electrons not originally inside the separatrix can become recaptured.

In this illustration, an axially symmetric electron beam and radiation beam are assumed. The wiggler has parabolic pole faces so that weak transverse focusing is the same in both the x and y planes. A total of 10 Gaussian-Laguerre modes were used in the simulation. The differences in results using 10 Gaussian-Laguerre modes versus 6 Gaussian-Laguerre modes is typically much less than 5%.

Figure 3 is a plot of the radiation spot size as a function of distance. In the absence of optical guiding, the Rayleigh length would be 3 m, and at the end of the interaction the radiation spot size would be 13 times larger than the initial spot size of 0.1 cm. As a result of optical guiding, the final spot size is only 0.32 cm. The radiation is therefore able to propagate through the vacuum chamber without significant loss, because the condition $g = 2.5\ cm\ > 5r_s + 0.3\ cm = 1.9\ cm$ is satisfied, where g is minimum wiggler gap[11].

Figure 4 is a plot of the radiation power in each mode as a function of axial distance. The fundamental mode clearly dominates and the SDE method is extremely accurate for evaluating the spot size and wave front curvature.

Figure 5 is a plot of the efficiency as a function of beam energy spread. For electron beams with energy spread less than 1.0% Gaussian full width, the smaller input radiation power gives a higher efficiency. This is a consequence of optical guiding. We have shown

in Ref. 6 that perfectly guided radiation beams cannot be maintained in the high-gain trapped-particle regime. However, the radiation is well-focused compared to free space diffraction. The envelope equation for the radiation beam has the form[6-7]

$$r_s'' + K^2 r_s = 0. \tag{22}$$

The parameter governing radiation focusing is

$$K^2 = \left(\frac{2c/\omega}{r_s^2}\right)^2 \left(-1 + C^2 < \sin\psi >^2 + 2C < \cos\psi > + \frac{\omega}{2c} r_s^2 C' < \sin\psi >\right), \tag{23}$$

where $C(z) = (2\nu/\gamma)(1-f)(1+f)^{-2}(a_w/|a_{0,0}(z)|)$ is the coupling coefficient, $f(z) = \sigma_b/\sigma_r$ is the filling factor, and $\sigma_r = \pi r_s^2$ is the area of the radiation beam. The first term on the right-hand side of (23) is defocusing and corresponds to the usual diffraction expansion, the second and third terms are always focusing while the last term is usually a defocusing contribution. For perfectly guided beams, $K^2 = 0$. For weakly guided beams, the focusing terms are reduced. The coupling coefficient C is larger when the initial input is smaller. Thus, the radiation focuses better when the input power is smaller. Figure 6 is a comparison of radiation spot sizes as a function of z for the input radiations of (—) 50 MW and (– –) 500MW obtained for simulations with no energy spread. The spot size associated with 50 MW input is smaller and the final efficiency is larger.

II. Single Stage Power Amplifier (SSPA)

A somewhat simpler configuration, that can achieve high power and high efficiency, is the single stage power amplifier (SSPA)[12]. In the SSPA configuration (see Fig. 1b), a low power laser, such as a dye laser, is directly amplified and optically guided in a uniform wiggler region until saturation occurs. The intrinsic efficiency in the uniform wiggler region is small, typically less than 2%. For efficiency enhancement, the wiggler is spatially tapered just prior to saturation. At this point the electron beam is tightly bunched in the ponderomotive wave, and the trapping potential can be sufficiently large. The SSPA configuration requires a slightly longer overall wiggler length. The main advantage of the SSPA configuration is the elimination of the high power master oscillator.

The parameters of the wiggler, the input radiation and the electron beam for the 1 μm SSPA configuration are given in Table II. The electron beam has an energy of 250 MeV, a peak current of 1 kA, an intrinsic energy spread of 1.0% FWHM, a normalized edge emittance of $\epsilon_n = 0.007\ cm\ rad$ and thus, a beam brightness $B = 5 \times 10^{11} A/(m - rad)^2$.

The following simulation results are obtained with an injected radiation beam power of 15 kW peak, focused at the entrance of the wiggler to a spot size of 0.11 cm. The free space Rayleigh length is 4 m. At exact resonance, the radiation saturates at a distance of 15 m with an intrinsic efficiency of 0.39%. At the end of the uniform wiggler region, the trapping potential is

$$\frac{|e|\phi_{trap}}{\gamma m_0 c^2} = 4\left(\frac{a_w a_{00}}{1 + a_w^2}\right)^{1/2} = 3.2\%.$$

In the uniform wiggler section, the radiation beam is optically guided and the magnetic field amplitude and period are 3.155 kG and 9.6 cm, respectively. The wiggler taper begins just prior to the saturation point ($z = 15\ m$). Figure 7 shows the taper of the amplitude of the vector potential of the wiggler. If all the electrons are trapped, the maximum efficiency would be 27%. A plot of the efficiency as a function of the axial distance is shown in Fig. 8. The maximum efficiency is 22% at the end of the wiggler and a substantial fraction of the beam electrons are trapped in the ponderomotive buckets. Figure 9 indicates that the wiggler can be tapered further to obtain even higher efficiencies. The spot size of the radiation field is plotted in Fig. 9. The spot size at the end of the wiggler is 0.24 cm.

Conclusions

With the recent advances in RF linac technology towards higher power and higher brightness, FEL configurations driven by RF linacs are no longer limited to oscillators. We have presented examples of the MOPA and SSPA configurations for achieving high FEL power and efficiency. The SSPA is the simpler of the two configurations because the high power master oscillator is replaced with a low power conventional laser source.

Acknowledgments

This work has been supported by ONR.

References

[1] P. Sprangle and C. M. Tang, Appl. Phys. Lett. 39, 677 (1981); AIAA J. 19, 1164 (1981); C. M. Tang and P. Sprangle, *Free-Electron Generator* of Coherent Radiation, Physics of Quantum Electronics, Vol. 9, eds., S. F. Jacobs, G. T. Moore, H. S. Pilloff, M. Sargent III, M. O. Scully, R. Spitzer (Edison-Wesley, Reading, MA, 1982) p. 627.

[2] G. T. Moore, Opt. Comm. 52, 46(1984), 54, 121 (1985).

[3] G. T. Moore, Nucl. Instr. and Methods in Phys. Res. 239, 19 (1985).

[4] E. T. Scharlemann, A. M. Sessler and J. S. Wurtele, Phys. Rev. Lett. 54, 1925 (1985).

[5] M. Xie and D. A. G. Deacon, Nucl. Instr. and Methods in Phys. Res. A250, 426 (1986).

[6] P. Sprangle, A. Ting and C. M. Tang, Phys. Rev. Lett. 59, 202 (1987); P. Sprangle, A. Ting and C. M. Tang, Phys. Rev. A30, 2773 (1987).

[7] P. Sprangle, A. Ting, B. Hafizi and C. M. Tang, Nucl. Instr. and Methods in Phys. Res. A272, 536, 1988.

[8] C. M. Tang and P. Sprangle, IEEE J. Quantum Electron., QE-21, 970(1985).

[9] E. T. Scharlemann, J. Appl. Phys., 58, 2154(1985).

[10] A. H. Stroud, *Approximate Calculation of Multiple Integrals,* Prentice-Hall, Inc., Englewood Cliffs, NJ, 1971, p. 293.

[11] K. Halbach, Journal De Physique, Colloque C1, supplement au n°2, Tome 44, 211 (1983).

[12] Private communications with L. Thode at LANL and D. Prosnitz at LLNL.

Table I

Parameters of Numerical Simulation in the MOPA Configuration

Electron Beam (parabolic density profile)	
Energy, E	140 MeV
Current, I	500 A
Intrinsic E-spread, $\Delta E/E$	1.0% (Gaussian full width)
Slippage distance	0.08 cm
Norm. edge emittance, ϵ_n	0.008 cm-rad
Radius, r_b	0.08 cm
Energy spread due to ϵ_n, $\frac{\Delta\gamma_z}{\gamma_z} = \frac{1}{2}\frac{\epsilon_n^2}{r_b^2}\frac{1}{1+a_w^2}$	0.17%
Wiggler (linearly polarized)	
Period, λ_w	5.0 cm
Init. magnetic field, B_w	4.28 kG
Final magnetic field, B_w	3.21 kG
Wiggler length, L_w	40 m
Initial normalized vector potential, a_w	$\sqrt{2}$
Taper (amplitude)	non-uniform (max 15.8%)
Radiation	
Wavelength, λ	1 μm
Input power, $P_{\rm in}$	50 MW
Min. spot size of input rad.	0.1 cm (at z = 0 m)
Initial Rayleigh length	3.0 m
Final spot size, r_s **(z=40 m)**	0.32 cm
Output power, $P_{\rm out}$ **(peak)**	5.2 GW
Efficiency at end of wiggler	7.5%

Table II

Parameters of Numerical Simulation in the Power Amplifier Configuration

Electron Beam (parabolic density profile)	
Energy, E	250 MeV
Current, I	1000 A
Intrinsic E-spread, $\Delta E/E$	1.0% (Gaussian full width)
Slippage distance	0.08 cm
Norm. edge emittance, ϵ_n	0.007 cm-rad
Radius, r_b	0.087 cm
Energy spread due to ϵ_n, $\frac{\Delta\gamma_z}{\gamma_z} = \frac{1}{2}\frac{\epsilon_n^2}{r_b^2}\frac{1}{1+a_w^2}$	0.06%
Wiggler (linearly polarized)	
Period, λ_w	9.6 cm
Init. magnetic field, B_w	3.155 kG
Final magnetic field, B_w	2.05 kG
Wiggler length, L_w	80 m
Initial normalized vector potential, a_w	2.0
Taper (amplitude)	non-uniform (max 27%)
Radiation	
Wavelength, λ	1 μm
Input power, $P_{\rm in}$	15 kW
Min. spot size of input rad.	0.11 cm (at z = 0 m)
Initial Rayleigh length	4.0 m
Final spot size, r_s (z=80 m)	0.23 cm
Output power, $P_{\rm out}$ (peak)	53 GW
Efficiency at end of wiggler	22%

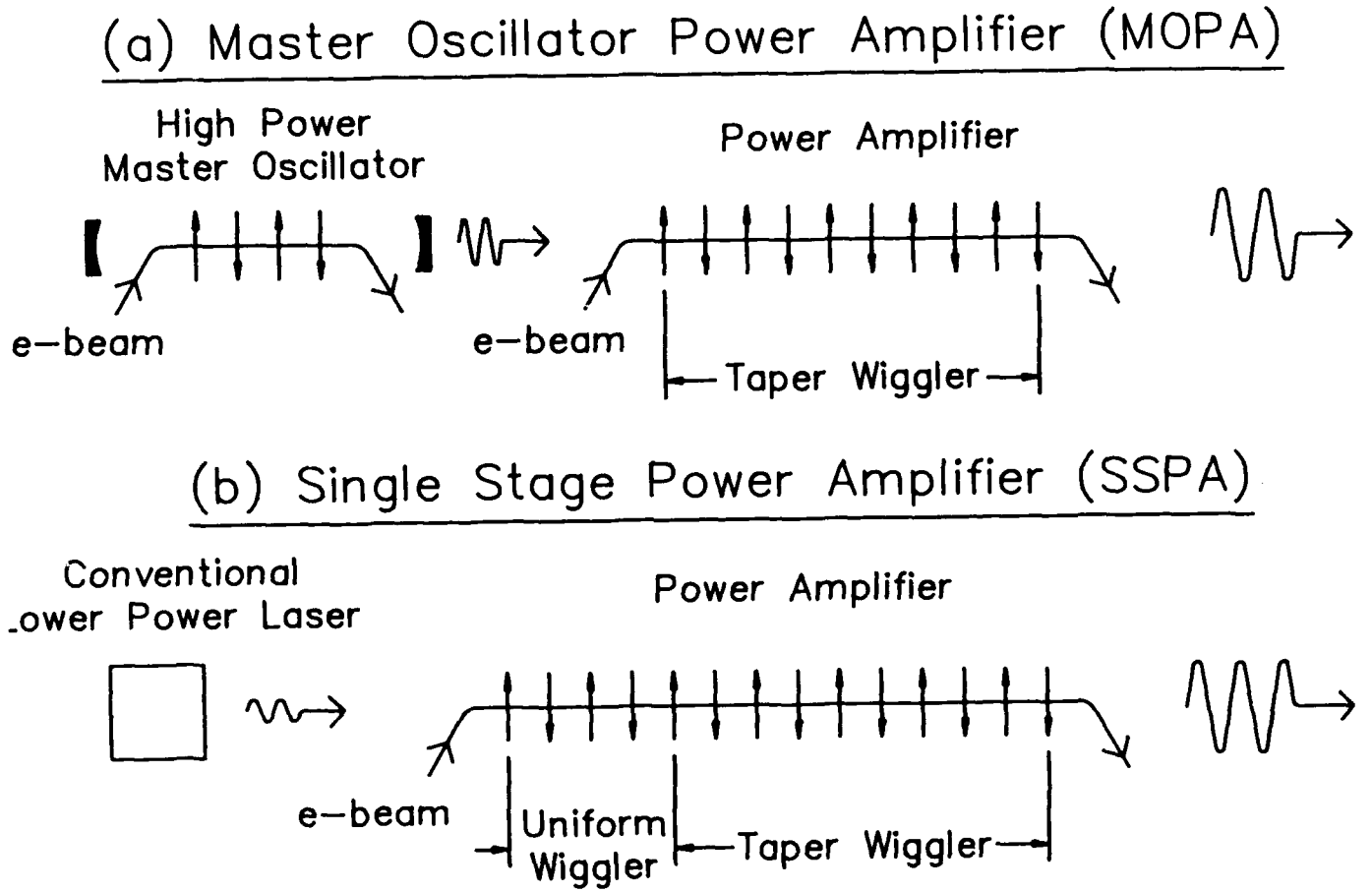

Fig. 1. Schematic diagram of (a) the master oscillator power amplifier (MOPA) configuration and (b) the single stage power amplifier (SSPA) configuration.

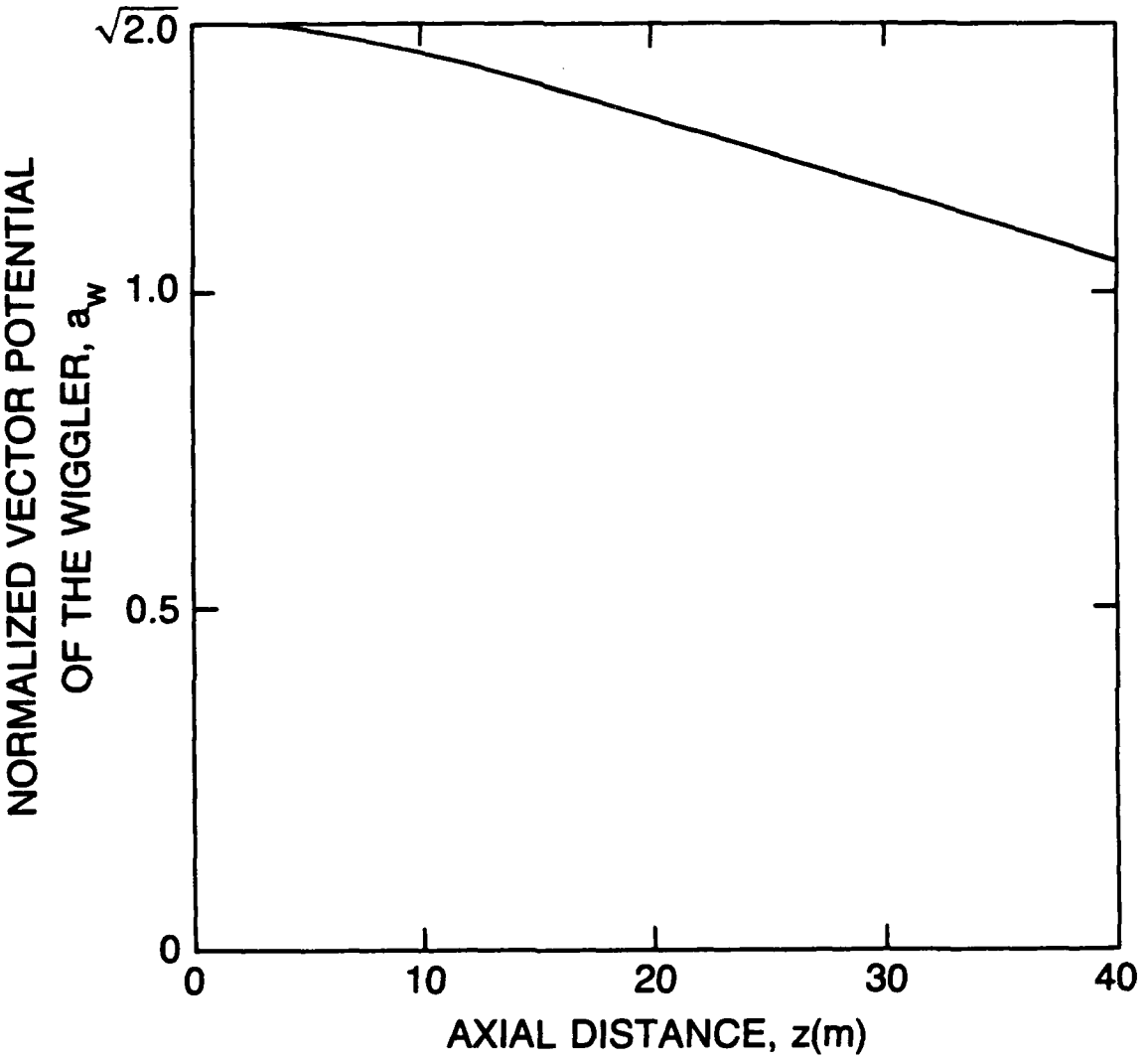

Fig. 2. Plot of the amplitude of the normalized vector potential of the wiggler as function of interaction distance z.

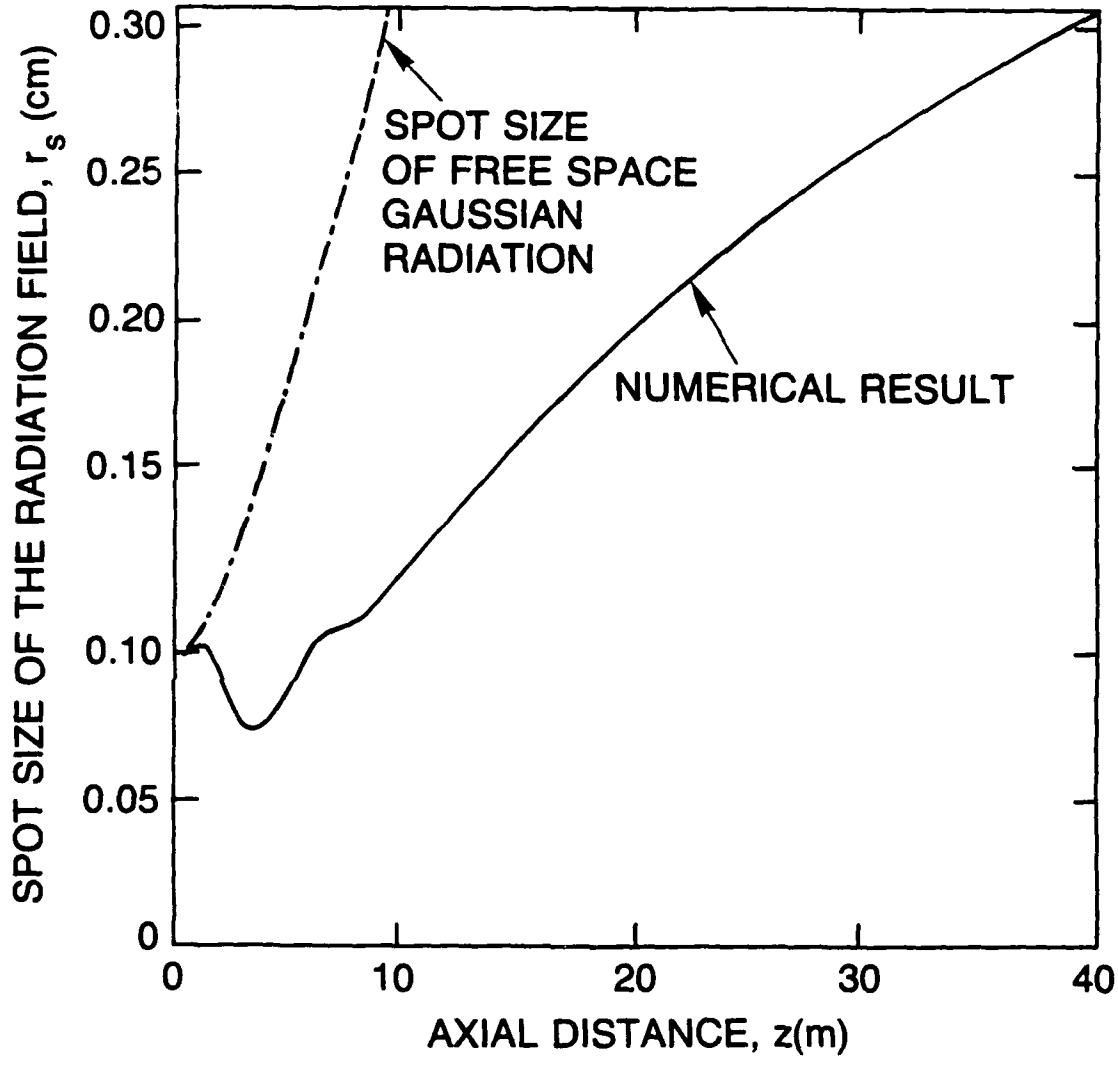

Fig. 3. Plot of the radiation spot size as a function of distance z for 1.0% Gaussian full width energy spread.

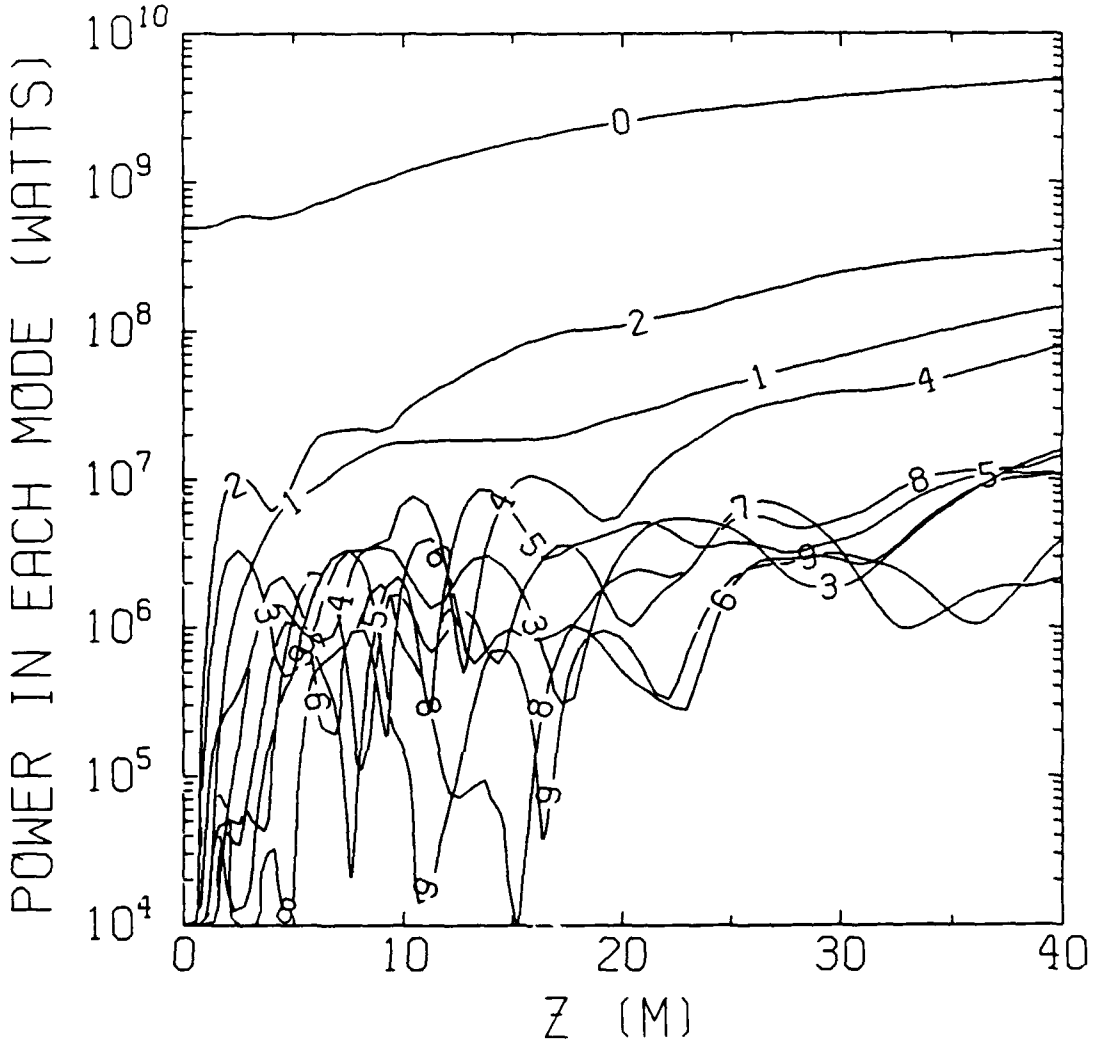

Fig. 4. Plot of radiation power for each mode as a function of distance with initial radiation input power of 50 MW.

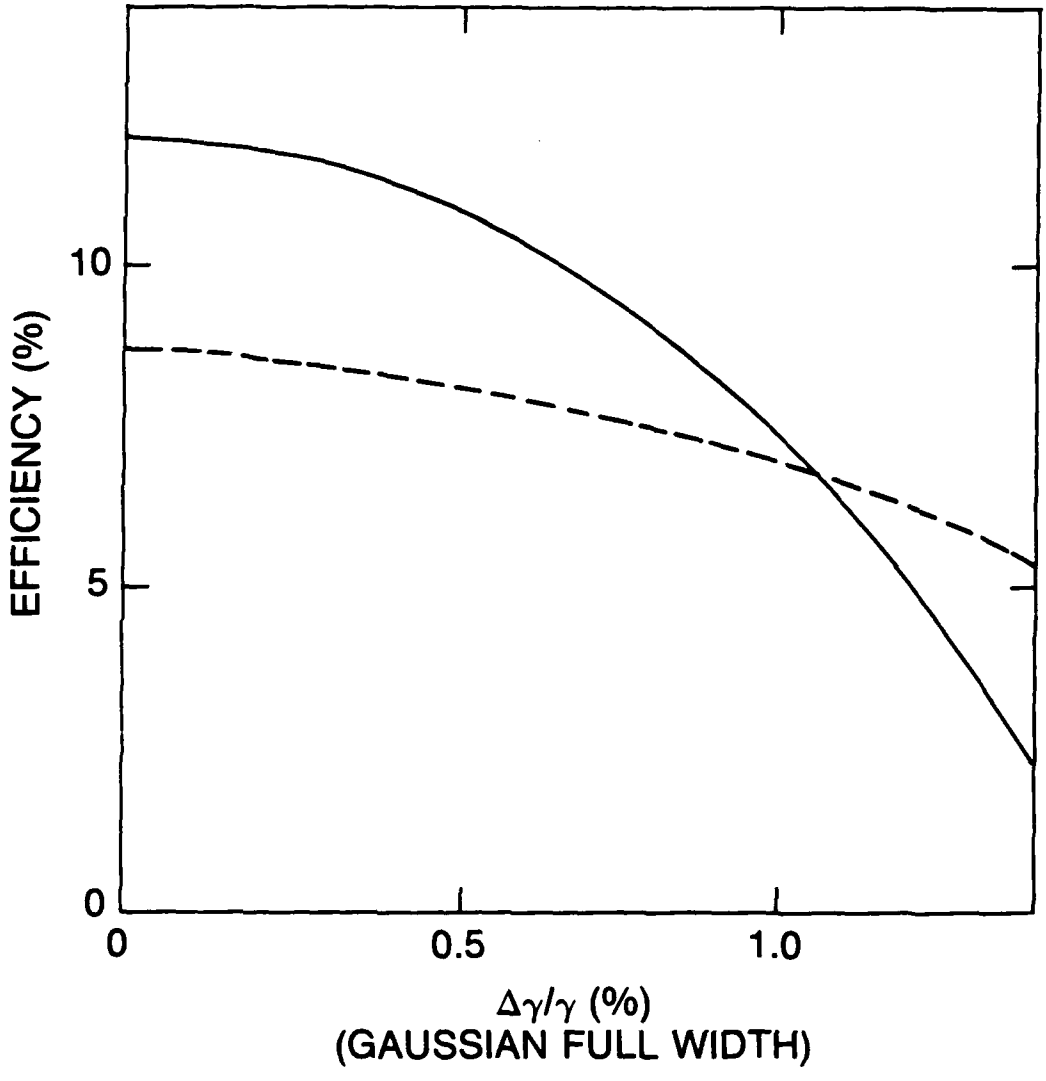

Fig. 5. Plot of the Efficiency as a function of energy spread for input radiation power of (—) 50 MW and (– –) 500 MW.

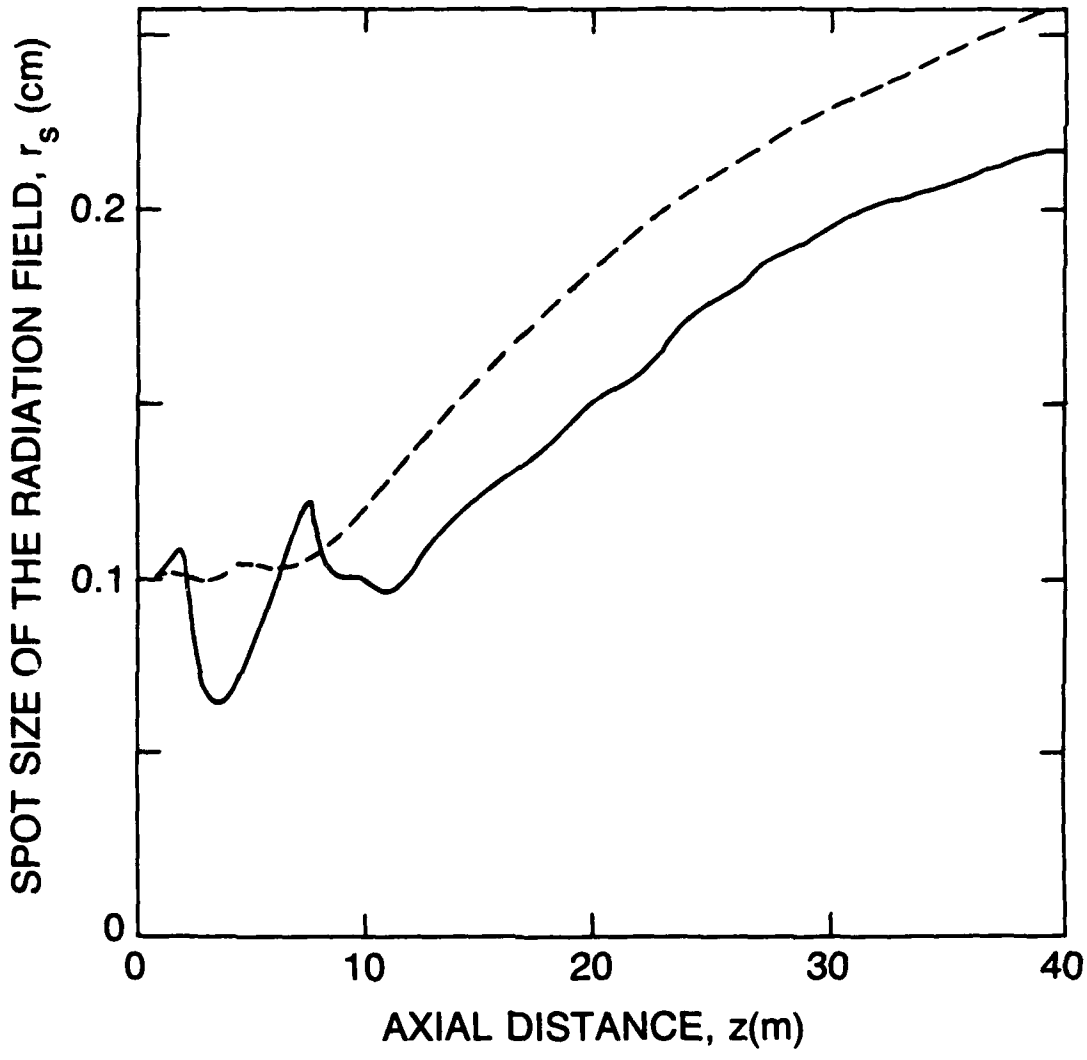

Fig. 6. Plots of spot sizes as a function of axial distance for an electron beam with no initial energy spread for input radiation power of (—) 50 MW and (– –) 500 MW.

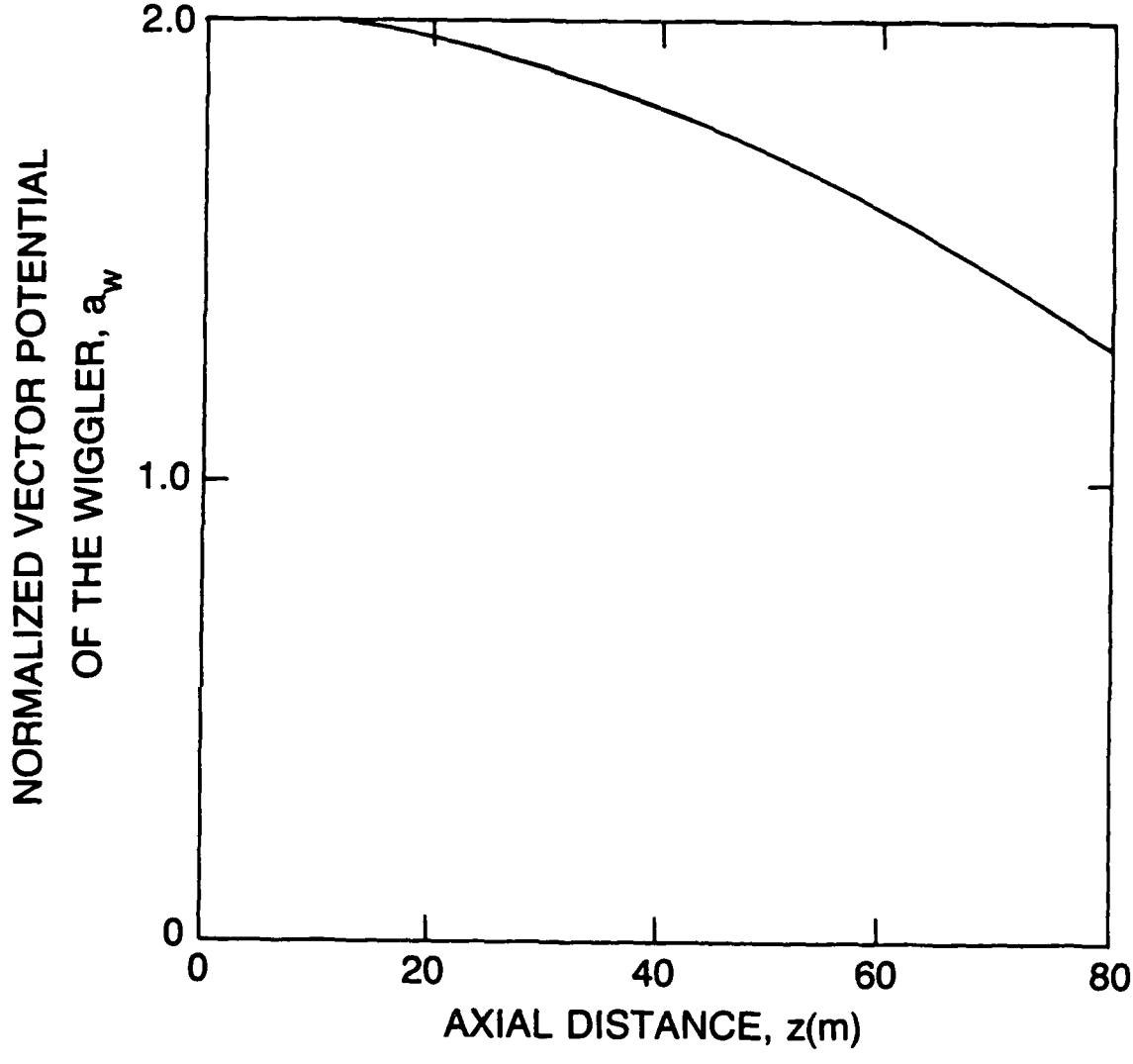

Fig. 7. Plot of the amplitude of the normalized vector potential of the wiggler as a function of interaction distance z.

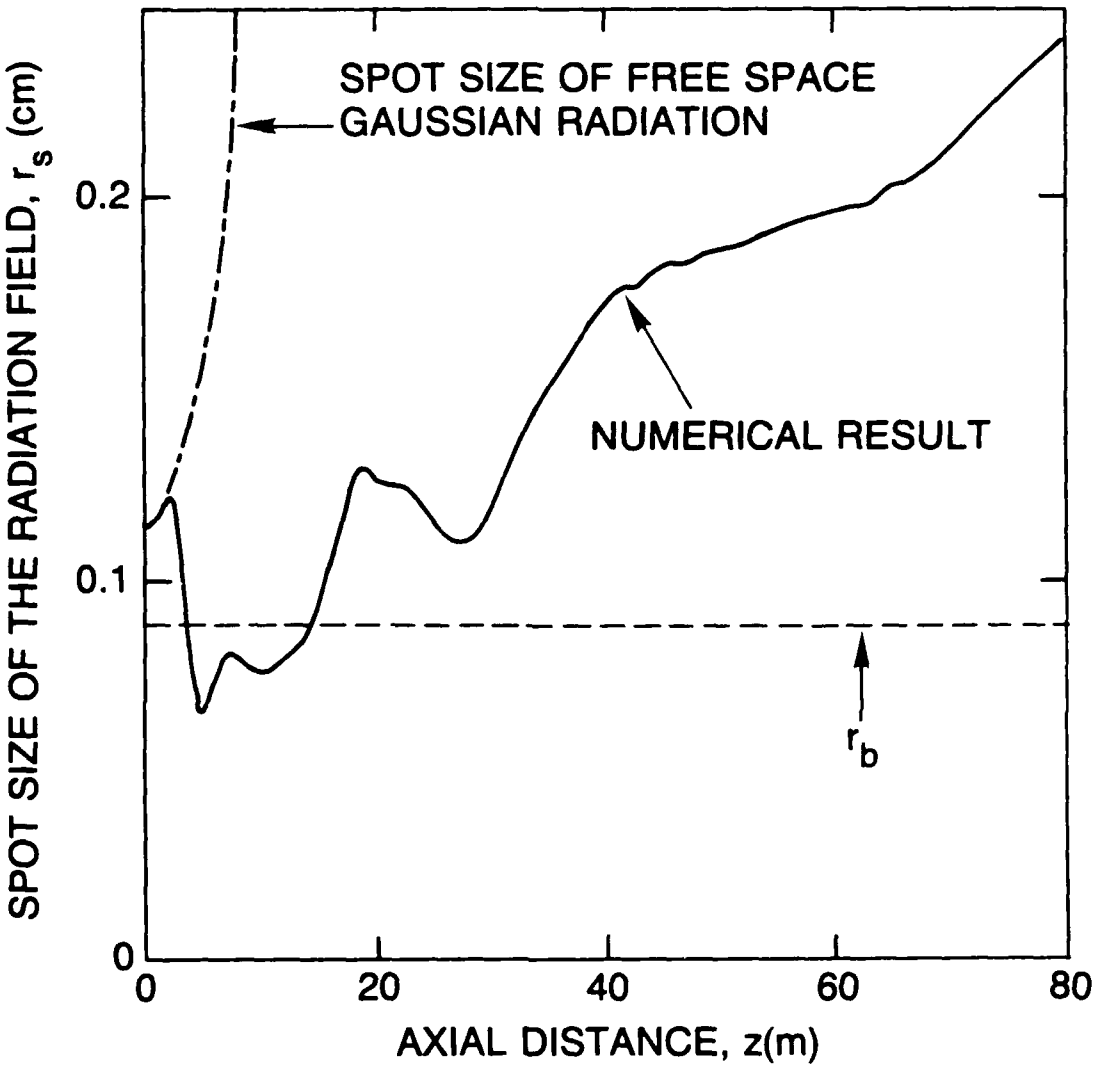

Fig. 8. Plot of the radiation spot size as a function of distance z for 1.0% Gaussian full width energy spread.

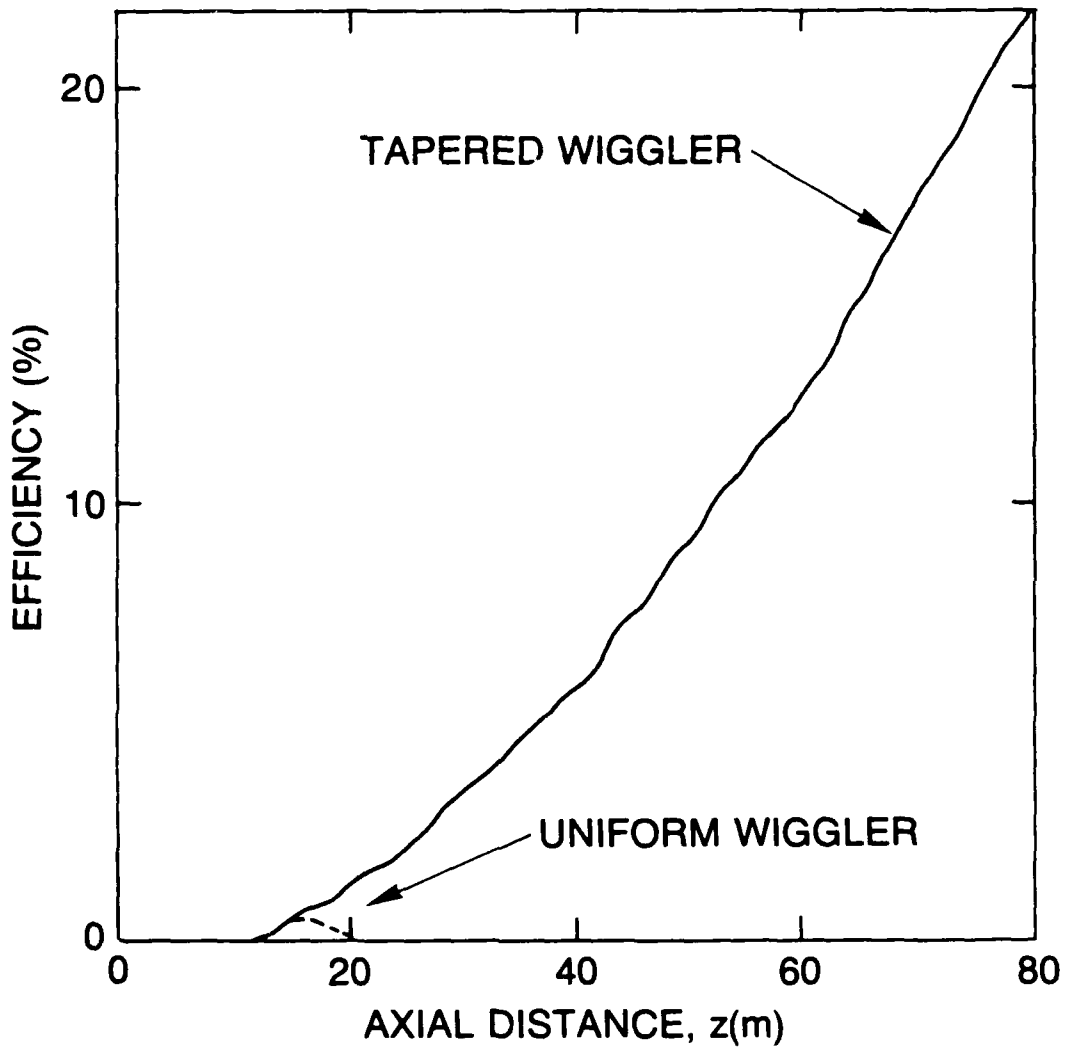

Fig. 9. Plot of efficiency as a function of the axial distance z.

DISTRIBUTION LIST

Naval Research Laboratory
4555 Overlook Avenue, S.W.
Washington, DC 20375-5000

Attn: Code 1000 - Commanding Officer, CAPT John J. Donegan, Jr.
1001 - Dr. T. Coffey
1005 - Head, Office of Management & Admin.
1005.1-Deputy Head, Office of Management & Admin.
1005.6-Head, Directives Staff
1200 - CAPT R. W. Michaux
1201 - Deputy Head, Command Support Division
1220 - Mr. M. Ferguson
2000 - Director of Technical Services
2604 - NRL Historian
3000 - Director of Business Operations
4000 - Dr. W. R. Ellis
0124 - ONR
4600 - Dr. D. Nagel
4603 - Dr. W. W. Zachary
4700 - Dr. S. Ossakow (26 copies)
4700.1-Dr A. W. Ali
4790 - Dr. P. Sprangle (25 copies)
4790 - Dr. C. A. Kapetanakos
4790 - Dr. J. Mathew
4730 - Dr. R. Elton
4707 - Dr. W. M. Manheimer
4790 - Dr. W. Black
4790 - Dr. A. W. Fliflet
4790 - Dr. S. Gold
4790 - Dr. D. L. Hardesty
4790 - Dr. A. K. Kinkead
4790 - Dr. M. Rhinewine
4770 - Dr. G. Cooperstein
4790 - Dr. C. M. Tang (25 copies)
4790 - Dr. G. Joyce
4790 - Dr. M. Lampe
4790 - Dr. Y. Y. Lau
4790 - Dr. A. Ting (25 copies)
4790 - Dr. E. Esarey
4790 - Dr. J. Krall
4790A- B. Pitcher (25 copies)
5700 - Dr. L. A. Cosby
5745 - Dr. J. Condon
6840 - Dr. S. Y. Ahn
6840 - Dr. A. Ganguly
6840 - Dr. R. K. Parker
6843 - Dr. R. H. Jackson
6843 - Dr. N. R. Vanderplaats
6843 - Dr. C. M. Armstrong
6875 - Dr. R. Wagner
2628 - *Documents* (22 copies)
2634 - D. Wilbanks

NOTE: Every name listed on distribution gets one copy except for those where extra copies are noted.

Dr. R. E. Aamodt
Lodestar Research Corp.
2400 Central Ave., P-5
Boulder, CO 80306-4545

Dr. J. Adamski
Boeing Aerospace Company
P.O. Box 3999
Seattle, WA 98124

Dr. T. M. Antonsen
University of Maryland
College Park, MD 20742

Assistant Secretary of the
Air Force (RD&L)
Room 4E856, The Pentagon
Washington, D.C. 20330

Dr. W. A. Barletta
Lawrence Livermore National Lab.
P. O. Box 808
Livermore, CA 94550

Dr. W. Becker
Univ. of New Mexico
Institute for Mod. Opt.
Albuquerque, NM 87131

Dr. Robert Behringer
9342 Balcon Ave.
Northridge, CA 91325

Dr. G. Bekefi
Mass. Institute of Tech.
Room 36-213
Cambridge, MA 02139

Dr. Steven V. Benson
Physics Building
Duke University
Durham, NC 27706

Dr. I. B. Bernstein
Mason Laboratory
Yale University
400 Temple Street
New Haven, CT 06520

Dr. Amitava Bhattacharjee
Columbia University
S. W. Mudd 210
Dept. of Applied Phys.
New York, NY 10027

Dr. Anup Bhowmik
Rockwell International/Rocketdyne Div.
6633 Canoga Avenue, FA-40
Canoga Park, CA 91304

Dr. G. Bourianoff
1901 Rutland Drive
Austin, TX 78758

Dr. Charles Brau
Vanderbilt University
Nashville, TN 37235

Dr. R. Briggs
SSC Laboratory
Stoneridge Office Park
2550 Beckleymeade Ave.
Suite 260
Dallas, TX 75237

Prof. William Case
Dept. of Physics
Grinnell College
Grinnell, IA 50112

Dr. R. Center
Spectra Tech., Inc.
2755 Northup Way
Bellevue, WA 98004

Dr. K. C. Chan
Los Alamos National Laboratory
P. O. Box 1663
Los Alamos, NM 87545

Prof. Frank Chen
School of Eng. & Applied Sciences
Univ. of Calif. at Los Angeles
7731 K Boelter Hall
Los Angeles, CA 90024

Dr. S. Chen
MIT Plasma Fusion Center
NW16-176
Cambridge, MA 01890

Dr. D. P. Chernin
Science Applications Intl. Corp.
1720 Goodridge Drive
McLean, VA 22102

Dr. William Colson
Berkeley Research Assoc.
P. O. Box 241
Berkeley, CA 94701

Dr. Richard Cooper
Los Alamos National Scientific
Laboratory
P.O. Box 1663
Los Alamos, NM 87545

Dr. R. A. Cover
Rockwell International/Rocketdyne Div.
6633 Canoga Avenue, FA-38
Canoga Park, CA 91304

Dr. Bruce Danly
MIT
NW16-174
Cambridge, MA 02139

Dr. R. Davidson
Plasma Fusion Center
Mass. Institute of Tech.
Cambridge, MA 02139

Dr. John Dawson
Physics Department
University of California
Los Angeles, CA 90024

Dr. David A. G. Deacon
Deacon Research
Suite 203
900 Welch Road
Palo Alto, CA 94304

Dr. Philip Debenham
Center for Radiation Research
National Bureau of Standards
Gaithersburg, MD 20899

Director
National Security Agency
Fort Meade, MD 20755
ATTN: Dr. Richard Foss, A42
Dr. Thomas Handel, A243
Dr. Robert Madden, R/SA

Director of Research (2 copies)
U. S. Naval Academy
Annapolis, MD 21402

Dr. A. Drobot
Science Applications Intl. Corp.
1710 Goodridge Road
McLean, VA 22102

Dr. Dwight Duston
SDIO/IST
The Pentagon
Washington, DC 20301-7100

Dr. J. A. Edighofter
TRW, Bldg. R-1
One Space Park
Redondo Beach, CA 90278

Dr. Luis R. Elias
Creol-FEL Research Pavillion
Suite 400
12424 Research Parkway
Orlando, FL 32826

Dr. C. James Elliott
X1-Division, M.S. 531
Los Alamos Natl. Scientific Lab.
P. O. Box 1663
Los Alamos, NM 87545

Dr. Anne-Marie Fauchet
Brookhaven National Laboratories
Associated Universities, Inc.
Upton, L.I., NY 11973

Dr. R. Gajewski
Div. of Advanced Energy Projects
U. S. Dept of Energy
Washington, DC 20545

Dr. J. Gallardo
Brookhaven National Laboratory
Associated Universities, Inc.
Upton, L.I., NY 11973

Dr. B. B. Godfrey,
Chief Scientist
WL/CA
Kirtland AFB, NM 87117-6008

Dr. John C. Goldstein, X-1
Los Alamos Natl. Scientific Lab.
P.O. Box 1663
Los Alamos, NM 87545

Dr. V. L. Granatstein
Dept. of Electrical Engineering
University of Maryland
College Park, MD 20742

Dr. K. Halbach
Lawrence Berkeley Laboratory
University of California, Berkeley
Berkeley, CA 94720

Dr. R. Harvey
Hughes Research Laboratory
3011 Malibu Canyon Road
Malibu, CA 90265

Prof. Herman A Haus
Mass. Institute of Technology
Rm. 36-351
Cambridge, MA 02139

Dr. B. Hui
Defense Advanced Research Projects Agency
1400 Wilson Blvd.
Arlington, VA 22209

Prof. V. Jaccarino
Univ. of Calif. at Santa Barbara
Santa Barbara, CA 93106

Dr. B. Carol Johnson
Ctr. for Radiation Research
National Inst. of Standards and Tech.
Gaithersburg, MD 20899

Dr. Ron Johnson
Ctr. for Radiatiuon Research
Natl. Inst. of Standards and Tech.
Gaithersburg, MD 20899

Dr. Shayne Johnston
Physics Department
Jackson State University
Jackson, MS 39217

Dr. R. A. Jong
Lawrence Livermore National Laboratory
P. O. Box 808/L626
Livermore, CA 94550

Dr. Howard Jory
Varian Associates, Bldg. 1
611 Hansen Way
Palo Alto, CA 94303

Dr. C. Joshi
University of California
Los Angeles, CA 90024

Dr. K. J. Kim, MS-101
Lawrence Berkeley Lab.
Rm. 223, B-80
Berkeley, CA 94720

Dr. Brian Kincaid
Lawrence Berkeley Laboratory
University of California, Berkeley
Berkeley, CA 94720

Prof. N. M. Kroll
Department of Physics
B-019, UCSD
La Jolla, CA 92093

Dr. Thomas Kwan
Los Alamos National Scientific
Laboratory, MS608
P. O. Box 1663
Los Alamos, NM 87545

Dr. J. LaSala
Physics Dept.
U. S. M. A.
West Point, NY 10996

Dr. Michael Lavan
U.S. Army Strategic Def. Command
ATTN: Code CSSD-H-D
P. O. Box 1500
Huntsville, AL 35807-3801

Dr. B. Levush
Dept. of Physics & Astronomy
University of Maryland
College Park, MD 20742

Dr. Anthony T. Lin
Dept. of Physics
University of California
Los Angeles, CA 90024

Dr. Chuan S. Liu
Dept. of Physics & Astronomy
University of Maryland
College Park, MD 20742

Dr. A. Luccio
Brookhaven National Laboratory
Accelerator Dept.
Upton, NY 11973

Prof. J.M.J. Madey
117 Physics Bldg.
Duke University
Durham, NC 27706

Dr. R. Mako
205 South Whiting Street
Alexandria, VA 22304

Dr. Joseph Mangano
Science Research Laboratory
1600 Wilson Blvd.
Suite 1200
Arlington, VA 22209

Dr. Siva A. Mani
Science Applications Intl. Corp.
1040 Waltham Street
Lexington, MA 02173-8027

Dr. T. C. Marshall
Applied Physics Department
Columbia University
New York, NY 10027

Dr. Xavier K. Maruyama
Dept. of Physics
Naval Postgraduate School
Monterey, CA 93943

Dr. B. McVey
Los Alamos National Laboratory
P. O. Box 1663
Los Alamos, NM 87545

Dr. David Merritt
Space & Naval Warfare Command
Attn: PMW 145A
Washington, DC 20363-5100

Dr. A. Mondelli
Science Applications Intl. Corp.
1710 Goodridge Drive
P.O. Box 1303
McLean, VA 22101

Dr. Mel Month
Brookhaven National Laboratories
Associated Universities, Inc.
Upton, L.I., NY 11973

Dr. Gerald T. Moore
University of New Mexico
Albuquerque, NM 87131

Dr. Philip Morton
Stanford Linear Accelerator Center
P.O. Box 4349
Stanford, CA 94305

Prof. J. Nation
224 Phillips Hall
School of Elec. Eng.
Cornell University
Ithaca, NY 14850

Dr. George Neil
TRW
One Space Park
Redondo Beach, CA 90278

Dr. Kelvin Neil
Lawrence Livermore National Lab.
Code L-321, P.O. Box 808
Livermore, CA 94550

Dr. Brian Newnam
MSJ 564
Los Alamos National Scientific Lab.
P.O. Box 1663
Los Alamos, NM 87545

Dr. T. Orzechowski
L-436
Lawrence Livermore National Lab.
P. O. Box 808
Livermore, CA 94550

Prof. E. Ott
Department of Physics
University of Maryland
College Park, MD 20742

OUSDRE (R&AT)
Room 3D1067, The Pentagon
Washington, D.C. 20301

Dr. Robert B. Palmer
Brookhaven National Laboratories
Associated Universities, Inc.
Upton, L.I., NY 11973

Dr. J. Palmer
Hughes Research Laboratory
Malibu, CA 90265

Dr. Richard H. Pantell
Stanford University
Stanford, CA 94305

Dr. Dennis Papadopoulos
Astronomy Department
University of Maryland
College Park, Md. 20742

Dr. John A. Pasour
Mission Research Laboratory
8560 Cinderbed Road
Suite 700
Newington, VA 22122

Dr. C. K. N. Patel
Bell Laboratories
Murray Hill, NJ 07974

Dr. Claudio Pellegrini
Brookhaven National Laboratory
Associated Universities, Inc.
Upton, L.I., NY 11973

Dr. S. Penner
Center for Radiation Research
Natl. Inst. of Standards and Tech.
Gaithersburg, MD 20899

Dr. M. Piestrup
Adelphi Technology
13800 Skyline Blvd. No. 2
Woodside, CA 94062

Dr. D. J. Pistoresi
Boeing Aerospace Company
P. O. Box 3999
Seattle, WA 98124-2499

Major E. W. Pogue
SDIO
The Pentagon, T-DE Rm. 1E180
Washington, DC 20301-7100

Major Donald Ponikvar
U. S. Army SDC
P. O. Box 15280
Arlington, VA 22245-0280

Dr. Donald Prosnitz
Lawrence Livermore National Lab.
Box 5511 L-626
Livermore, CA 94550

Dr. D. C. Quimby
Spectra Technology
2755 Northup Way
Bellevue, WA 98004

Dr. G. Ramian
Quantum Institute
University of California
Santa Barbara, CA 93106

Dr. M. Reiser
University of Maryland
Department of Physics
College Park, MD 20742

Dr. S. Ride
Arms Control
Stanford University
Stanford, CA 94305

Dr. C. W. Roberson
Office of Naval Research
Code 112S
800 N. Quincy Street
Arlington, VA 22217

Dr. K. Robinson
Spectra Technology
2755 Northup Way
Bellevue, WA 98004

Dr. Marshall N. Rosenbluth
Dept. of Physics
B-019
Univ. of Calif., San Diego
LaJolla, CA 92093

Dr. J. B. Rosenzweig
The Inst. for Accelerator Physics
Department of Physics
University of Wisconsin-Madison
Madison, WI 53706

Dr. N. Rostoker
Department of Physics
University of California at Irvine
Irvine, CA 92717

Dr. A. Saxman
Los Alamos National Scientific Lab.
P. O. Box 1663, MSE523
Los Alamos, NM 87545

Dr. E. T. Scharlemann
L626
Lawrence Livermore National Laboratory
P. O. Box 808
Livermore, CA 94550

Prof. S. P. Schlesinger
Dept. of Electrical Engineering
Columbia University
New York, NY 10027

Dr. Howard Schlossberg
AFOSR
Bolling AFB
Washington, D.C. 20332

Dr. George Schmidt
Stevens Institute of Technology
Physics Department
Hoboken, NJ 07030

Dr. M. J. Schmitt
Los Alamos National Laboratory
P. O. Box 1663
Los Alamos, NM 87545

Dr. H. Schwettmann
Phys. Dept. & High Energy
Physics Laboratory
Stanford University
Stanford, CA 94305

Dr. Marlan O. Scully
Dept. of Physics & Astronomy
Univ. of New Mexico
800 Yale Blvd. NE
Albuquerque, NM 87131

Dr. S. B. Segall
KMS Fusion
3941 Research Park Dr.
P.O. Box 1567
Ann Arbor, MI 48106

Prof. P. Serafim
Northeastern University
Boston, MA 02115

Dr. A. M. Sessler
Lawrence Berkeley Laboratory
University of California
1 Cyclotron Road
Berkeley, CA 94720

Dr. W. Sharp
L-626
Lawrence Livermore National Laboratory
P. O. Box 808
Livermore, CA 94550

Dr. Earl D. Shaw
Bell Laboratories
600 Mountain Avenue
Murray Hill, NJ 07974

Dr. R. L. Sheffield
Los Alamos National Laboratory
P.O. Box 1663
Los Alamos, NM 87545

Dr. D. Shoffstall
Boeing Aerospace Company
P.O. Box 3999
Seattle, WA 98124

Dr. Jack Slater
Spectra Technology
2755 Northup Way
Bellevue, WA 98004

Dr. Todd Smith
Hansen Labs
Stanford University
Stanford, CA 94305

Dr. R. Sudan
Lab. of Plasma Studies
Cornell University
Ithaca, NY 14850

Dr. David F. Sutter
ER 224, GTN
Department of Energy
Washington, D.C. 20545

Dr. T. Tajima
Institute for Fusion Studies
University of Texas at Austin
Austin, TX 78712

Dr. R. Temkin
Mass. Institute of Technology
Plasma Fusion Center
Cambridge, MA 02139

Dr. L. Thode
Los Alamos National Laboratory
P.O. Box 1663
Los Alamos, NM 87545

Dr. Norman H. Tolk
Physics Department
Vanderbilt University
Nashville, TN 37240

Dr. Kang Tsang
Science Applications Intl. Corp.
1710 Goodridge Dr.
McLean, VA 22102

Dr. H. S. Uhm
Naval Surface Warfare Center
White Oak Lab.
Silver Spring, MD 20903-5000

Under Secretary of Defense (R&D)
Office of the Secretary of Defense
Room 3E1006, The Pentagon
Washington, D.C. 20301

Dr. John E. Walsh
Wilder Laboratory
Department of Physics (HB 6127)
Dartmouth College
Hanover NH 03755

Dr. Jiunn-Ming Wang
Brookhaven National Laboratories
Associated Universities, Inc.
Upton, L.I., NY 11973

Dr. Roger W. Warren
Los Alamos National Scientific Lab.
P.O. Box 1663
Los Alamos, NM 87545

Dr. J. Watson
Los Alamos National Laboratory
P. O. Box 1663
Los Alamos, NM 87545

Dr. Mark Wilson
Natl. Inst. of Standards and Tech.
Bldg. 245, Rm. B-119
Gaithersburg, MD 20899

Dr. J. Wurtele
M.I.T.
NW 16-234
Plasma Fusion Center
Cambridge, MA 02139

Dr. Ming Xie
Dept. of Physics
Stanford University
Stanford, CA 94305

Dr. Yi-Ton Yan
Stanford Linear Accelerator Center
P. O. 4349
Stanford, CA 94305

Dr. Simon S. Yu
Lawrence Livermore National Laboratory
P. O. Box 808
Livermore, CA 94550

Do NOT make labels
for these two-below:
Records---(1 copy)

Naval Research Laboratory
Washington, DC 20375-5000
Code 2630
Timothy Calderwood